

Dynamics of particles accelerated by head-on collisions of two magnetized plasma shocks

Cite as: Phys. Plasmas **25**, 022111 (2018); <https://doi.org/10.1063/1.5020180>

Submitted: 20 December 2017 • Accepted: 24 January 2018 • Published Online: 12 February 2018

Satoshi Takeuchi



View Online



Export Citation



CrossMark

ARTICLES YOU MAY BE INTERESTED IN

[Effect of polarization force on head-on collision between multi-solitons in dusty plasma](#)

Physics of Plasmas **25**, 033705 (2018); <https://doi.org/10.1063/1.5020194>

[Arbitrary amplitude nucleus-acoustic solitons in multi-ion quantum plasmas with relativistically degenerate electrons](#)

Physics of Plasmas **25**, 022110 (2018); <https://doi.org/10.1063/1.5023302>

[Cylindrical fast magnetosonic solitary waves in quantum degenerate electron-positron-ion plasma](#)

Physics of Plasmas **25**, 022308 (2018); <https://doi.org/10.1063/1.5007155>

Physics of Plasmas

Special Topic: Plasma Physics
of the Sun in Honor of Eugene Parker

Submit Today!



Dynamics of particles accelerated by head-on collisions of two magnetized plasma shocks

Satoshi Takeuchi^{a)}

Life and Environmental Science, University of Yamanashi, 4-4-37 Takeda, Kofu, Yamanashi 400-8510, Japan

(Received 20 December 2017; accepted 24 January 2018; published online 12 February 2018)

A kinetic model of the head-on collision of two magnetized plasma shocks is analyzed theoretically and in numerical calculations. When two plasmas with anti-parallel magnetic fields collide, they generate magnetic reconnection and form a motional electric field at the front of the collision region. This field accelerates the particles sandwiched between both shock fronts to extremely high energy. As they accelerate, the particles are bent by the transverse magnetic field crossing the magnetic neutral sheet, and their energy gains are reduced. In the numerical calculations, the dynamics of many test particles were modeled through the relativistic equations of motion. The attainable energy gain was obtained by multiplying three parameters: the propagation speed of the shock, the magnitude of the magnetic field, and the acceleration time of the test particle. This mechanism for generating high-energy particles is applicable over a wide range of spatial scales, from laboratory to interstellar plasmas. *Published by AIP Publishing.* <https://doi.org/10.1063/1.5020180>

I. INTRODUCTION

Numerous types of shock waves exist in interstellar plasmas. Supernova remnants (SNRs), pulsar wind nebulae, and active galactic nuclei would act as accelerators to create particles with high energy. Magnetotail or bow shock of planets, solar flares, and coronal mass ejection^{1,2} have been recognized as efficient mechanisms to generate high energy particles. In these phenomena, the shock waves interact with another shock or interstellar magnetic field in collisionless plasmas. When two plasmas possessing anti-parallel magnetic field collide with each other as shock waves, the magnetic reconnection is created playing an important role in high energy particle generation.

Magnetic reconnection has been confirmed in many laboratory-scale plasmas, observations of interstellar plasmas, and magnetohydrodynamic (MHD) and particle (PIC/Hybrid) simulation studies. MHD simulations conveniently elucidate the energy conversion processes from a macroscopic viewpoint. However, because MHD theory treats plasmas as magnetized fluids, it cannot sufficiently explain the significant microscopic dynamics such as the trapping and acceleration of particles. In contrast, PIC simulations simulate plasma shocks by reflecting plasma particles at a boundary³ or by forcing a change in the plasma density.⁴ Although these processes are microscopic, they are not easily generalizable to an arbitrary configuration of the shock fields. In addition, the calculation time and memory resources drastically increase in large simulation systems.

High energy electrons have been generated in various simulations of magnetic reconnections. The magnetic energy released in the reconnection region is effectively converted into kinetic and internal plasma energy. Nevertheless, the mechanism by which particles are accelerated to high energy remains an open question.

From a microscopic perspective, the present article investigates the fundamental features of the acceleration mechanism and the energy conversion process in two colliding plasmas. The interactions between individual plasma particles and the electromagnetic shock fields are revealed in numerical calculations. The kinetic model is a plausible candidate for clarifying particle behaviors such as trapping and acceleration.

II. MODEL OF PLASMA SHOCK

Let us consider a moving cloud of collisionless plasma confined in a magnetic field. The plasma consists of perfectly ionized gases in a quasi-neutral state. When the magnetized plasma moves, the magnetic field simultaneously generates a motional electric field. The movement of both fields with the plasma is known as the *frozen-in state*. Furthermore, as the electromagnetic fields satisfy Maxwell's equations, they are assumed to satisfy the superposition principle in collisionless plasmas. To clearly understand the basic concepts of two colliding plasma shocks, we focus on the following simple model.

Suppose that two magnetized plasmas with anti-parallel magnetic fields approach and collide, as shown in Fig. 1. The velocity of the plasma cloud is the vector product of the electric field \mathbf{E} and the magnetic field \mathbf{B} , namely, $\mathbf{v}/c = -\mathbf{E} \times \mathbf{B}/|\mathbf{B}|^2$ where c is the velocity of light.⁵

In configuring the electromagnetic fields of the plasma shocks, we assume uniform physical quantities in the x direction and the approach of two plasma shocks along the y direction. For a magnetic field in the yz plane, the electric fields in the y and z directions should be zero, i.e., $E_y = E_z = 0$.

The shape of the shock with magnetic field B_{zi} is expressed as follows:

$$B_{zi} = \frac{B_i}{2} \left[\tanh \eta_i + (-1)^i \right], \quad (1)$$

^{a)}Electronic mail: take@yamanashi.ac.jp

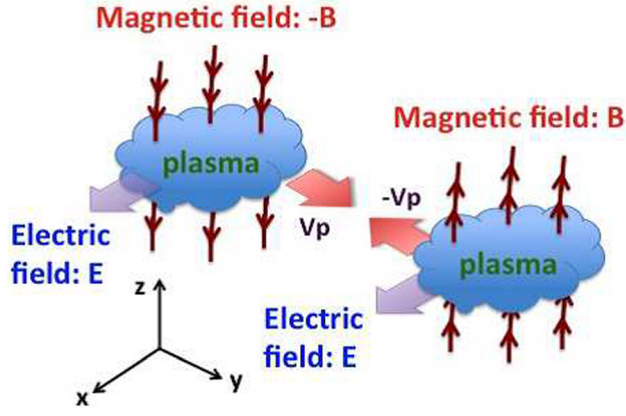


FIG. 1. Schematic of the head-on collision between two magnetized plasma clouds.

$$\eta_i \equiv k_i(y + v_i t) + h_i(z) + \phi_i, \quad (2)$$

where η_i is the phase parameter of the plasma shock, v_i is the propagation speed, k_i is the wave number, and ϕ_i is the phase constant. The subscript i is 1 for forward propagation and 2 for backward propagation (in the y direction). The magnitude of the magnetic field is given by $B_1 = B_2 \equiv B_0$.

The function $h_i(z)$ specifies the geometry of the magnetic field line. In a Petschek-type magnetic reconnection,^{6,7} the magnetic field line is given by a hyperbolic function in the reconnection region, which is approximately described by $h_i(\zeta) \approx (-1)^i \alpha \zeta^2$. Here, $\zeta \equiv kz$ and α denotes the coefficient of the magnetic field line with the radius of curvature $\tilde{R} \equiv (2\alpha)^{-1}$. The electron cyclotron frequency is given by $\omega_{ce} \equiv qB_0/m_e c$ and the width of the shock front is $k^{-1} \equiv c/\omega_{ce}$.^{8–10}

The other field components of the plasma shock are derived from Faraday's law of induction and the relation $\nabla \cdot \mathbf{B} = 0$:

$$B_{yi} = -\frac{d\eta_i}{d\zeta} B_{zi} = -\frac{B_0}{2} \frac{dh_i}{d\zeta} \left[\tanh \eta_i + (-1)^i \right], \quad (3)$$

$$E_{xi} = -\frac{v_i B_0}{2c} \left[\tanh \eta_i + (-1)^i \right]. \quad (4)$$

The electromagnetic fields of the shocks were configured as shown in Fig. 2. The colored and non-colored regions are occupied by magnetized and non-magnetized plasmas, respectively.

III. BASIC EQUATIONS OF MOTION

The relativistic equation of motion of a test particle with mass m_e and charge q is given by

$$m_e \frac{d\gamma \mathbf{v}}{dt} = q\mathbf{E} + \frac{q}{c} \mathbf{v} \times \mathbf{B}, \quad (5)$$

where $\gamma \equiv [1 - (v_x^2 + v_y^2 + v_z^2)/c^2]^{-1/2}$ is the Lorentz factor. The total field is considered as the superposition between two plasma fields. For simplicity, the fields are considered to be symmetric about the xz plane; i.e., $v_2 = -v_1 \equiv v_p$, $h_1 = -h_2 \equiv h$, and $\phi_1 = -\phi_2 \equiv \phi$. As a result, the definite fields can be written as

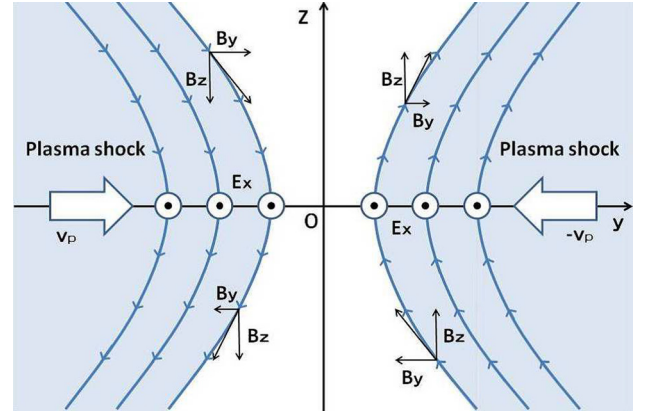


FIG. 2. Model of the two colliding plasma shocks. The electric field E_x is symmetric with respect to the xz plane, and the magnetic field B_y and B_z components are anti-parallel with respect to the xy plane and xz plane, respectively.

$$E_x^t \equiv E_{x1} + E_{x2} = -\frac{v_p B_0}{2c} (\tanh \eta_1 - \tanh \eta_2 - 2), \quad (6)$$

$$B_y^t \equiv B_{y1} + B_{y2} = -\alpha \zeta B_0 (\tanh \eta_1 - \tanh \eta_2 - 2), \quad (7)$$

$$B_z^t \equiv B_{z1} + B_{z2} = \frac{B_0}{2} (\tanh \eta_1 + \tanh \eta_2). \quad (8)$$

By the use of non-dimensional forms as follows:

$$(\tilde{E}_x^t, \tilde{B}_y^t, \tilde{B}_z^t) \equiv (E_x^t, B_y^t, B_z^t)/B_0, \quad (9)$$

$$\tau \equiv \omega_{ce} t, \quad \beta_j \equiv v_j/c, \quad (j = x, y, z), \quad (10)$$

the equations of motion can be rewritten in simple forms

$$\frac{d\gamma \beta_x}{d\tau} = \tilde{E}_x^t + (\beta_y \tilde{B}_z^t - \beta_z \tilde{B}_y^t), \quad (11)$$

$$\frac{d\gamma \beta_y}{d\tau} = -\beta_x \tilde{B}_z^t, \quad (12)$$

$$\frac{d\gamma \beta_z}{d\tau} = -\beta_x \tilde{B}_y^t. \quad (13)$$

The equation relating to the (energy) gain derived from Eqs. (11)–(13) is given by

$$\frac{d\gamma}{d\tau} = \tilde{E}_x^t \beta_x. \quad (14)$$

The non-dimensional form of these equations is beneficial in both theoretical and numerical analyses.

IV. KINETIC ANALYSIS

To clarify the features of the particle acceleration in the above model, we use the zeroth-order approximation around the center of the collision region. Substituting $\eta = 0$ and $\zeta = 0$ into Eqs. (6)–(8) under the condition $\beta_p \tau > 1$, the fields are represented as $\tilde{B}_z^t = \tilde{B}_y^t = 0$ and $\tilde{E}_x^t = 2\beta_p$. The magnetic neutral sheet and the motional electric field are generated near the center of the collision region, as previously indicated in the MHD model.¹¹ Particles are reportedly trapped around the neutral sheet and meander in the trapping

region.¹² In the present model, the test particle is also trapped by the neutral sheet and accelerated by the motional electric field E_x^t along that sheet.

In the above approximation, integrating Eq. (14) with respect to time gives the (energy) gain

$$\gamma \approx 2\beta_p \tau \equiv 2 \left(\frac{v_p}{c} \right) \left(\frac{qB_0}{m_e c} \right) t, \quad (15)$$

where $\beta_x \approx 1$ is assumed for the accelerating particle. Therefore, the particle obtains significant gain provided that it remains within the neutral sheet. The acceleration mechanism is similar to that of magnetic trapping acceleration (MTA) investigated by the present author.^{13–15} However, such efficient acceleration cannot continue indefinitely. During the acceleration, the particle's trajectory is bent by the Lorentz force imparted by the magnetic field \tilde{B}_y^t in the neutral sheet. Accordingly, the gain of the test particle is rapidly saturated.

To investigate this saturation analytically, we apply a first-order approximation to the magnetic fields, i.e., $\tilde{B}_y^t = 2\alpha\zeta$ and $\tilde{B}_z^t = 0$. Using Eq. (15) and the expression $\beta_x \approx 1$, Eq. (13) can be rewritten as

$$\frac{d^2\zeta}{d\tau^2} + \frac{1}{\tau} \frac{d\zeta}{d\tau} - \frac{2\alpha\zeta}{\beta_p \tau} = 0. \quad (16)$$

Solving this expression, we obtain $\zeta_0 I_0(\mu)$ with $\mu \equiv \sqrt{8\alpha\tau/\beta_p}$, where I_0 is the zeroth-order modified Bessel function of the first kind and ζ_0 is the initial position at $\tau = 0$. The z component of the particle velocity is given by

$$\beta_z = \frac{d\zeta}{d\mu} \frac{d\mu}{d\tau} \equiv \frac{4\alpha\zeta_0 I_1(\mu)}{\beta_p \mu}, \quad (17)$$

where $I_1(\mu) = dI_0(\mu)/d\mu$.

According to Eq. (14), the energy gain saturates at $\beta_x = 0$. Defining τ_s as the initial time of energy saturation, the attainable energy gain of the particle is $G_s \equiv mc^2 \gamma_a = mc^2 \cdot 2\beta_p \tau_s$. Substituting $\beta_z \approx 1$ into Eq. (17) and expanding the function I_1 with respect to μ , i.e., $I_1 \approx \mu^3/16$, the attainable gain becomes

$$\gamma_a = 2\beta_p \tau_s \approx \frac{\beta_p^3}{\alpha^2 \zeta_0} \equiv 4 \frac{\beta_p^3}{\zeta_0} \tilde{R}^2. \quad (18)$$

The above theoretical derivations suggest some features. For instance, the (energy) gain increases with increasing strength of the magnetic field B_0 [see Eq. (15)]. Meanwhile, the attainable (energy) gain γ_a depends not on the magnetic field, but on the radius of curvature \tilde{R} . Therefore, if the two colliding plasmas have a uniform shock front (i.e., $\alpha = 0$ or $\tilde{R} = \infty$), all particles near the collision region are trapped by the magnetic neutral sheet and accelerated infinitely. The particle initially located at the center of the collision region also gains energy continuously because $\zeta_0 = 0$ is a singular point. At a large value of μ , the approximation $I_1(\mu)/\mu \sim \exp(\mu)/\mu^{3/2}$ is established. It indicates that the singularity

is weaker for larger τ than for small $\tau \sim 1/\zeta_0$. It would become a mechanism of selective particle accelerations.

V. NUMERICAL CALCULATIONS

As the relativistic equations of motion are nonlinear, they preclude explicit solutions for the particle motions. Therefore, the theoretical analysis was complemented by numerical simulations of the normalized relativistic equations of motion [Eqs. (11)–(13)]. The calculations were carried out by the Runge-Kutta-Gill method.

The traveling speed of the plasma shock, the magnetic field strength, and the parabolic coefficient were assumed as $\beta_p = 0.2$, $B_1/B_2 = 1$, and $\alpha_i = 0.05$, respectively. The initial positions (η_0, ζ_0) of the test particles were randomly placed within the rectangular area centered on the collision region, i.e., $(-10 \leq \eta_0 \leq 10, -10 \leq \zeta_0 \leq 10)$.

The initial velocity of a test particle at its initial position (η_0, ζ_0) was given as the transport velocity $\beta_0(\eta_0, \zeta_0) = \mathbf{B}(\eta_0, \zeta_0) \times \mathbf{E}(\eta_0, \zeta_0)/|\mathbf{B}|^2$. Therefore, the test particles move with the electromagnetic fields of the shocks, whose configurations are mathematically described. In the present model, the calculation parameters of the plasma shock can be changed and the calculation time is reasonable.

A. Energy gain of particles

Figure 3 shows the time evolution of the (energy) gain of the test particles. The theoretical gain (straight line in Fig. 3) is given by Eq. (15). The numerically computed energy gain rate is consistent with the theoretical rate, meaning that the accelerating test particles experience the same electric field $\tilde{E}_x^t = 2\beta_p$. During the acceleration, the particles near the collision region are pushed outside by the acceleration region, so their energy gains become constant. The value of constant energy gain is called the *saturation gain* γ_s .

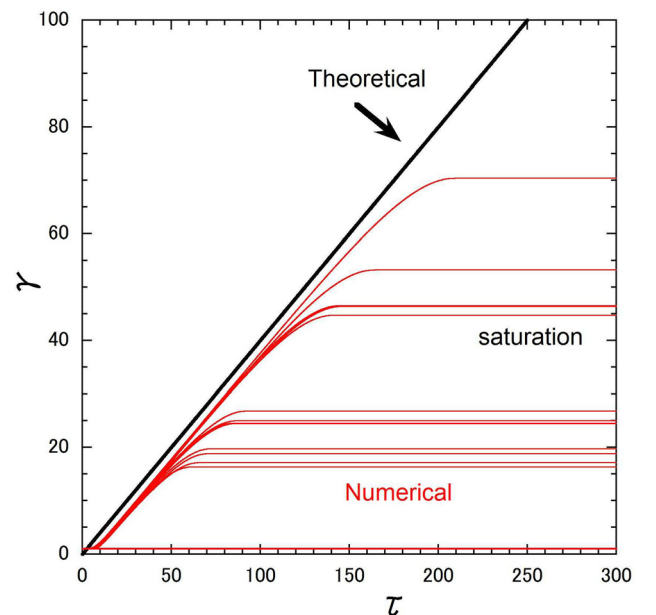


FIG. 3. Time evolutions of the energy gains of test particles accelerated by a motional electric field.

B. Attainable energy

Persistent energy gain of the particle is theoretically possible as described above. To investigate the relations between the attainable gain γ_a and the three parameters α , β_p , and ζ_0 , we traced the trajectories of many test particles until their gains become constant in which the initial position of the test particles was fixed at $(\xi_0, \eta_0) = (0, 0)$.

Figure 4 plots the saturation gains γ_s at different initial positions ζ_0 as a function of α . Increasing the radius of curvature $\tilde{R} = (2\alpha)^{-1}$ reduced the value of α , implying that the magnetic neutral region created by the reconnection expanded more widely at faster speed. In this situation, the particles inside the neutral region continued to be accelerated, and their attainable (energy) gain increased. As shown in Fig. 4, the saturation gain γ_s decreases linearly with α . As the traveling speed β_p of the shock is constant, the relation $\gamma_s \propto \alpha^{-1.23}$ is derived.

Figure 5 plots the saturation gain γ_s versus initial position ζ_0 of the test particles at different traveling speeds. The gain decreases with increasing ζ_0 , reflecting the distance of the particle from the collision region. If ζ_0 is small, the particle is accelerated continuously. The linear relationship is obtained as $\gamma_s \propto \zeta_0^{-0.28}$.

The saturation gains γ_s for various values of β_p are plotted in Fig. 6. The particles approach each other at the speed of the plasma shock. When the two shocks collide head-on, the (energy) gains of the test particles increase rapidly as the traveling speed of the shock approaches the velocity of light, indicating an effective relativistic effect. When α is fixed, the relation $\gamma_s \propto \beta_p^{2.20}$ is obtained.

Common to all these three figures, the saturation gain linearly increased or decreased on a logarithmic scale as the variable parameter increased on a linear scale. To explicitly relate the gain to these three parameters (α , β_p , ζ_0), the most probable saturation gain γ_p was obtained by the multiple regression method. The result was

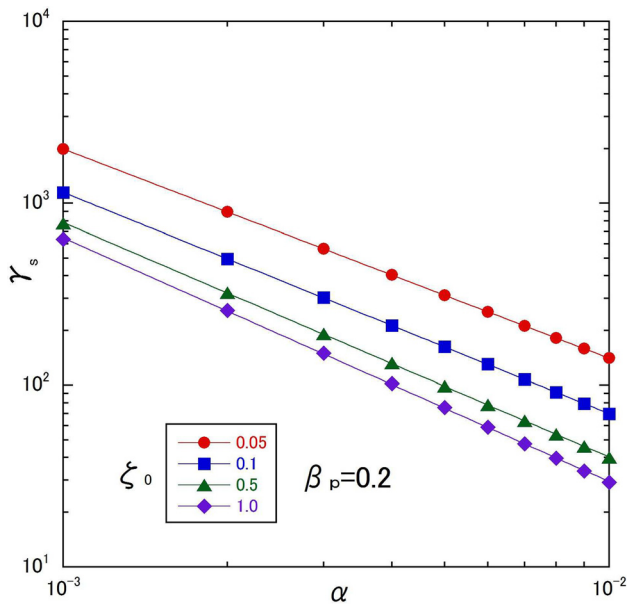


FIG. 4. Relation between the saturation gain γ_s and coefficient α . The saturation gain increases with decreasing initial position ζ_0 .

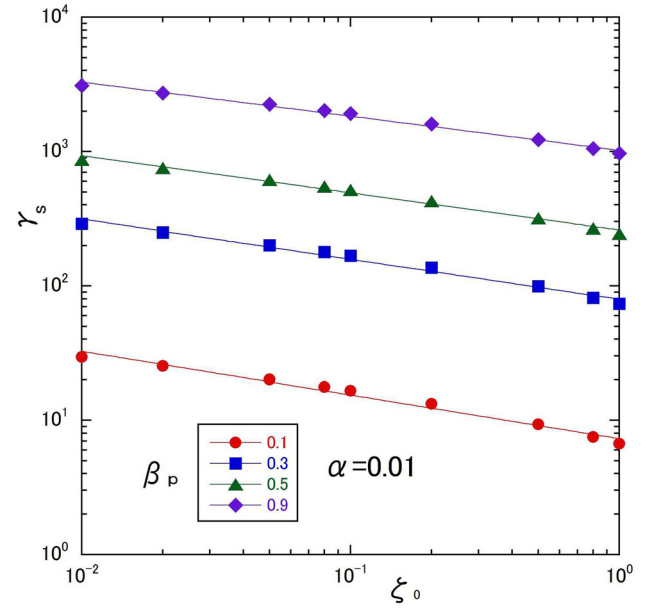


FIG. 5. Relation between saturation gain γ_s and initial position ζ_0 . The saturation gain increases with increasing speed β_p . The coefficient α is constant.

$$\gamma_p = \frac{3.89\beta_p^{2.20}}{\alpha^{1.23}\zeta_0^{0.28}}, \quad (19)$$

where the relative error between γ_s and γ_p (given by $|\gamma_p - \gamma_s|/\gamma_s$) is 9.6%.

C. Particle dynamics

To investigate the accelerations of the test particles from a microscopic viewpoint, we traced the motions of the test particles located near the shock front in the early stages of the numerical calculations.

Figure 7(a) traces the accelerating and drifting particles. The three-dimensional trajectories of the test particles are

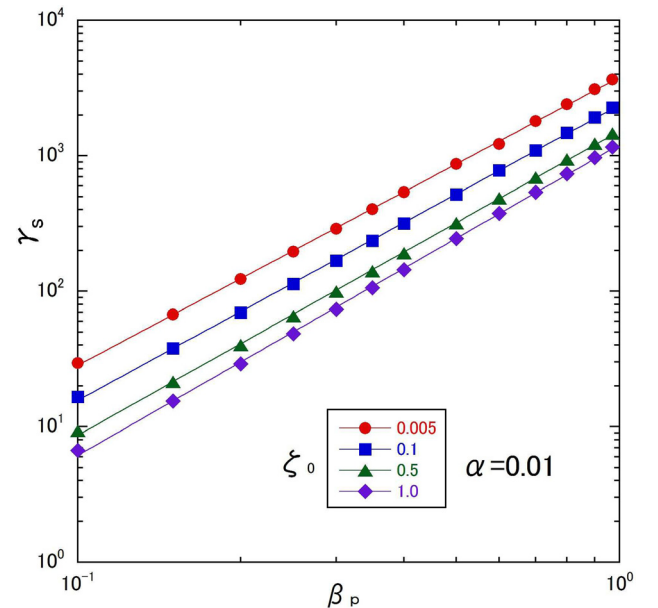


FIG. 6. Relation between saturation gain γ_s and traveling speed β_p . The saturation gain increases with decreasing initial position ζ_0 .

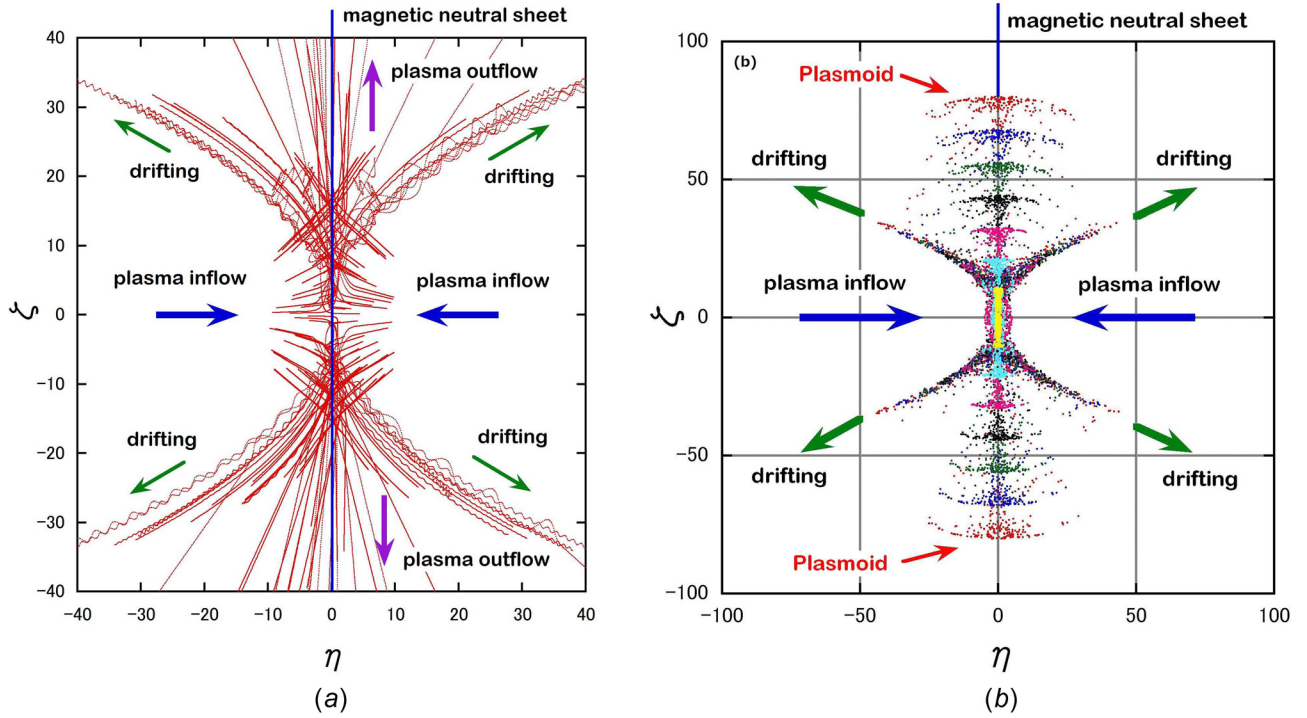


FIG. 7. Time evolution of the particle trajectories and distributions on the $\eta\zeta$ plane. The magnetic neutral sheet is located at $\eta = 0$. (a) Head-on collision of the two plasma shocks. (b) Snapshot of the plasmoid ejected from the collision region. The earliest and latest times of the evolution are encoded in yellow and red, respectively.

projected onto the $\eta\zeta$ plane. A left-inflowing plasma collides with a right-flowing plasma in the center of the figure. During this head-on collision, a magnetic neutral sheet was eventually created and a motional electric field $\tilde{E}_x^t = 2\beta_p$ was generated in the positive ζ direction, accelerating some of the particles near the collision region along the neutral sheet. As the acceleration proceeded, the particle trajectories were bent by the transverse magnetic field and the particles were pushed outside the acceleration region. Accordingly, their (energy) gains were gradually reduced. Their trajectories appeared as anti-parallel plasma outflows along the magnetic neutral sheet. Furthermore, the transverse field bent the trajectories of other particles beyond the collision region, carrying them along the curved magnetic field. Thus, the transverse magnetic field imparts a magnetic resistivity.

Figure 7(b) is a snapshot of the collective motions projected on the $\eta\zeta$ plane. Initially, all particles are located near the center of the area sandwiched between the two shocks. As the head-on collision was symmetric, the particle distributions were almost symmetric when projected in both the $\zeta\eta$ and $\zeta\zeta$ planes. Clusters of test particles (called plasmoids) moved to the upper and lower sides as time elapsed. The particles in these plasmoids were accelerated by the motional electric field and bent by the transverse magnetic field. The plasmoid was ejected from the collision region once only, at an early stage of the collision. The other particles, with gyration motions, drifted along the curved magnetic field of the plasma surface, forming an x-shaped plot in Fig. 7(b).

Figure 8(a) plots the time evolutions of the trajectories projected onto the $\zeta\zeta$ plane. Remarkably, some particles initially located around $(\zeta_0, \eta_0) = (0, 0)$ were accelerated in the positive ζ direction by the motional electric field. A few

particles were even accelerated continuously, as described by Eq. (15). The energy gains of these selectively accelerated particles were very high, exceeding those of plasmoids. However, while accelerating those particles the transverse magnetic field crossing the neutral sheet was also experienced, which drove them in the positive or negative ζ direction as time elapsed. Meanwhile, the non-accelerated particles drifted by gyrating along the curved magnetic field.

Figure 8(b) is a snapshot of the collective motion of the particles distributed on the $\zeta\zeta$ plane. Two distinctive features appear in the ζ direction: asymmetry in the plasmoid distributions and a low number of accelerating particles. These phenomena are also caused by the motional electric field.

Figure 9(a) illustrates the time evolutions of the trajectories projected onto the $\zeta\eta$ plane. The shock plasmas inflowed toward the center from the top and bottom sides. Although a few particles were accelerated along the neutral sheet in the ζ direction, many of the particles drifted with gyration about the positive or negative η direction.

Figure 9(b) is the snapshot of the collective motions of the particles distributed on the $\zeta\eta$ plane. Overlapped particle distributions radiated in certain directions from the center of the collision region. A few particles were accelerated along the magnetic neutral sheet in the positive ζ direction. The plasmoid ejection (which characterizes the head-on collision) cannot be identified from this projection of the particle distribution.

VI. DISCUSSION AND SUMMARY

The electromagnetic fields of the two magnetized plasma shocks are calculated by a mathematical expression. Therefore, the electromagnetic fields induced by the accelerating particles

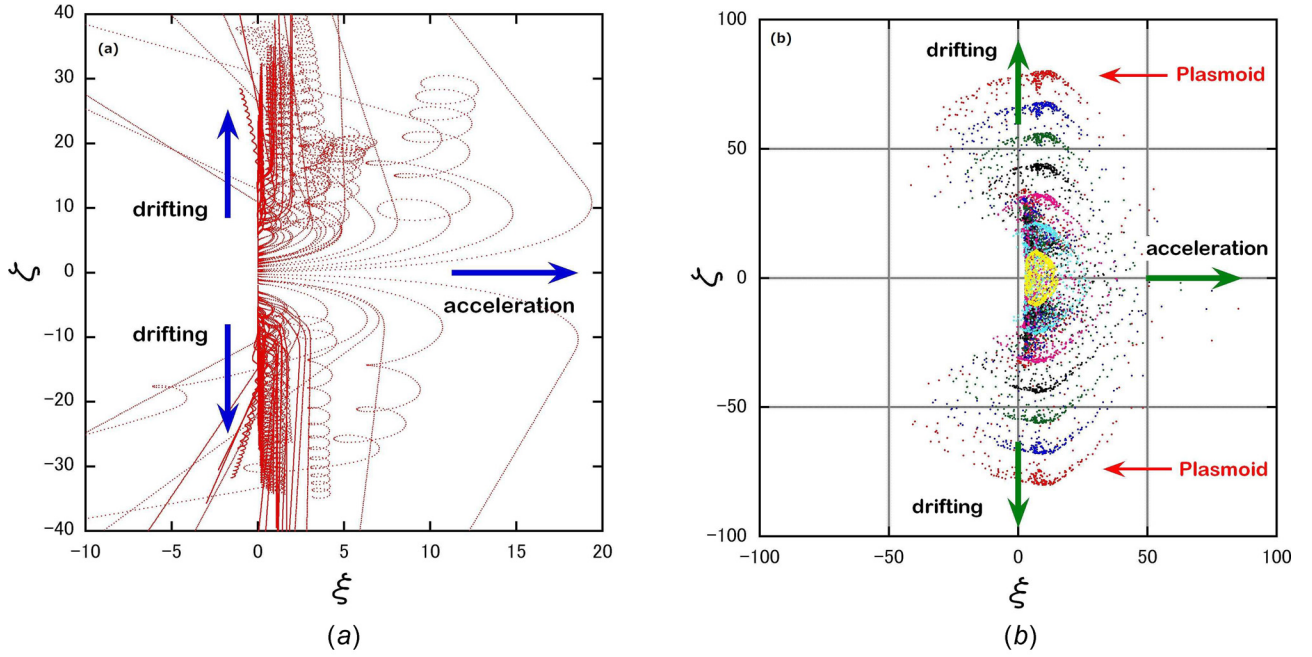


FIG. 8. Time evolution of the particle trajectories and distributions on the $\xi\zeta$ plane. (a) Cyclotron motions and acceleration of a few particles along the ξ axis. (b) Snapshot of the particle distributions with an asymmetric shape along the ξ axis.

cannot be generated self-consistently. Nonetheless, the model is useful for understanding the essence of magnetic reconnection in three dimensions. Furthermore, much of the information relating to head-on collisions can be obtained by surveying the parameters, which are easily exchanged in each calculation, and tested within a reasonable calculation time. Mathematical models describing the particle accelerations and magnetic reconnection in collisionless plasmas plasma fields have been applied in recent studies.^{16,19–22}

The particle trajectories and distributions provide much visual information on the accelerating and drifting particles.

The snapshot of particle distributions reveals the time evolution of the plasmoid. The plasmoid is ejected once in the early stage of the head-on collision, and cannot be identified in certain projection planes of the particle distributions.

Magnetic reconnection in magnetized collisionless plasmas is also associated with an anomalous resistivity. In MHD theory, energy dissipation has been explained by Ohmic resistivity associated with electron-ion collisions. In the present model, we show that anomalous resistivity might arise from the curved magnetic field near the collision region. This phenomenon, inferred as a dissipation mechanism in the magnetic

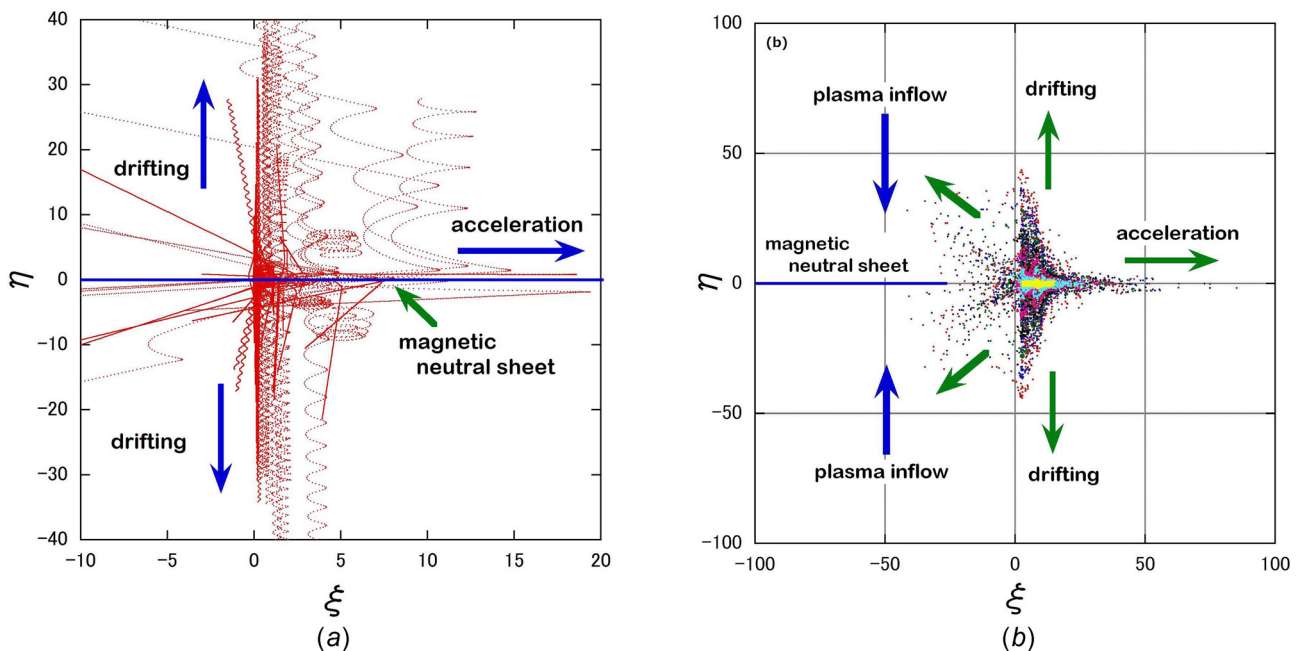


FIG. 9. Time evolution of the particle trajectories and distributions on the $\xi\eta$ plane. The magnetic neutral sheet is located at $\eta = 0$. (a) Cyclotron motions and acceleration of a few particles along the ξ axis. (b) Snapshot of the particle distributions. No plasmoid is observed.

reconnection, is similar to transverse magnetoresistivity in solid state physics. If stochastic or chaotic behaviors of particles exist around the neutral sheet, it would be a reason for resistivity in collisionless plasmas.^{17,18}

In the theoretical analysis, some test particles were continuously accelerated by the head-on collision. The numerically calculated energy gains of these accelerating particles agree well with the theoretical gains. The attainable gains of these particles depend on three parameters as shown in Eqs. (18) and (19). However, these parameters cannot sufficiently explain the features of magnetic reconnection in real plasmas.

To properly evaluate the attainable energy, let us exploit Eq. (15), which is adaptable to high-energy phenomena in experiments and observations.⁹ High-energy ions, electrons, or both are observed in laboratory experiments of magnetic reconnection.¹ Other interesting phenomena that generate high-energy particles through magnetic reconnection are solar flares,¹⁹ magnetotails of the Earth^{20,23} and Jupiter,²⁴ plasma jets,²⁵ and supernova remnants (SNRs).²⁶

Now, the energy gain $W \equiv m_e c^2 \gamma$ of a test particle is calculated as

$$W = 600 \left(\frac{v_s}{\text{cm/s}} \right) \left(\frac{B_0}{\text{G}} \right) \left(\frac{t_{acc}}{\text{s}} \right) \text{eV}, \quad (20)$$

where v_s and B_0 are the traveling speed and the magnetic field of the plasma shock, respectively. The acceleration time t_{acc} defines the time interval in which the particle gains its attainable energy. Suppose that the plasma shock travels at the Alfvén speed v_A (i.e., $v_s \equiv v_A$), and the acceleration time is the ion inertial length c/ω_{pi} divided by v_A , (i.e., $t_{acc} = c/\omega_{pi}v_A \equiv \omega_{ci}^{-1}$ where ω_{pi} and ω_{ci} are the ion plasma frequency and the ion cyclotron frequency, respectively). The acceleration time depends only on the magnitude of the magnetic field. Under these conditions, the attainable energy is calculated as $W = 2m_e c v_A \approx 1.87(v_A/c) \text{ GeV}$. This useful expression is applicable to various plasmas (but not to SNRs).

Table I shows the attainable energy gains of various laboratory and interstellar plasmas. Note that the acceleration times are relatively short and the attainable energies overestimated those of real plasmas, but are within the acceptable range.

For SNRs, we assumed the typical parameters (those of SN1006). If the acceleration time is 1 year, the acceleration is quick and typifies a young SNR²⁶ with a thin, filamentary shock-front structure.^{27–29} In this scenario, the propagation

TABLE I. Attainable energy gains of various plasmas calculated by Eq. (20). MRX: Magnetic Reconnection Experiment, RFP: Reversed Field Pinch, SNR: supernova remnant. Alfvén speed: $v_A \equiv B_0/\sqrt{4\pi m_i \rho}$, m_i : ion mass, ρ : plasma density.

Plasmas	ρ (cm^{-3})	B_0 (G)	v_A (cm/s)	t_{acc} (s)	W (eV)
MRX	10^{14}	10^2	2.2×10^6	10^{-6}	1.3×10^5
RFP	5×10^{13}	10^2	3.0×10^6	10^{-6}	1.9×10^5
Magnetotail	1.0	2×10^{-4}	4.3×10^7	0.5	2.7×10^6
Solar Corona	10^{11}	10^3	6.8×10^8	10^{-7}	4.3×10^7
SNR	5×10^{-6}	3×10^{-6}	2.9×10^8	3.2×10^7	1.6×10^{13}

and acceleration distances are $\Delta y = v_A t_{acc} \approx 6.7 \times 10^{-2} \text{ pc}$ and $\Delta x = c t_{acc} \approx 0.3 \text{ pc}$, respectively.

When one of the two colliding plasmas has a smaller magnetic field than the other and both fields intersect at any angle, the above mechanism should be replaced by our previously proposed field-aligned acceleration (FAA),^{9,10} another candidate mechanism of ultra-high energy acceleration in the universe.

In summary, a kinetic model of head-on collisions of two plasmas was presented in the relativistic regime. The particles were accelerated to high energy by the motional electric field in the collision region. However, the accelerating particles were also bent by the transverse magnetic field crossing the magnetic neutral sheet, so their energy gains saturated during the acceleration. The mathematical descriptions of two plasma shocks were interpreted and visualized in numerical simulations. A plasmoid was observed in the early stage of the head-on collision. The attainable energy gains of the accelerated particles were estimated over a wide size scale of plasmas, from laboratory to interstellar.

¹M. Yamada, R. Kulsrud, and H. Ji, *Rev. Mod. Phys.* **82**, 603 (2010).

²I. Roth and S. D. Bale, *J. Geophys. Res.* **111**, A07S06, <https://doi.org/10.1029/2005JA011434> (2006).

³M. Hoshino, *Prog. Theor. Phys. Suppl.* **143**, 149 (2001).

⁴Y. Ohsawa, *Phys. Fluids* **28**, 2130 (1985).

⁵J. D. Jackson, *Classical Electrodynamics*, 2nd ed. (John Wiley & Sons, New York, 1975), p. 473.

⁶B. U. Ö. Sonnerup, in *Solar System Plasma Physics*, edited by L. T. Lanzerotti, C. F. Kennel, and E. N. Parker (North-Holland Publishing Company, 1979), Vol. III, pp. 46–108.

⁷D. Biskamp, *Magnetic Reconnection in Plasmas* (Cambridge University Press, New York, 2000).

⁸S. Takeuchi, in *Magnetodynamic Phenomena in the Solar Atmosphere - Prototypes of Stellar Magnetic Activity*, edited by Y. Uchiyama, T. Kosugi, and H. S. Hudson (Kluwer Academic Publishers, 1996), pp. 581–582.

⁹S. Takeuchi, *Phys. Plasmas* **19**, 070703 (2012).

¹⁰S. Takeuchi, *Phys. Lett. A* **380**, 211 (2016).

¹¹T. Sato, T. Hayashi, K. Watanabe, R. Horiuchi, M. Tanaka, N. Sawairi, and K. Kusano, *Phys. Fluids B* **4**, 450 (1992).

¹²P. W. Seymour, *Aust. J. Phys.* **12**, 309 (1959).

¹³S. Takeuchi, K. Sakai, M. Matsumoto, and R. Sugihara, *Phys. Lett. A* **122**, 257 (1987).

¹⁴S. Takeuchi, *Phys. Rev. E* **66**, 037402 (2002).

¹⁵S. Takeuchi, *Phys. Plasmas* **12**, 102901 (2005).

¹⁶F. Mackay, R. Marchand, K. Kabin, and J. Y. Lu, *J. Plasma Phys.* **74**, 301 (2008).

¹⁷E. Horton and T. Tajima, *Geophys. Res. Lett.* **17**, 123, <https://doi.org/10.1029/GL017i002p00123> (1990).

¹⁸R. Numata and Z. Yoshida, *Phys. Rev. Lett.* **88**, 045003-1 (2002).

¹⁹M. Gordovskyy and P. K. Browning, *Astrophys. J.* **729**, 101 (2011).

²⁰A. Y. Ukhorskiy, M. I. Sitnov, V. G. Merkin, and A. V. Artemyev, *J. Geophys. Res.* **118**, 4952, <https://doi.org/10.1002/jgra.50452> (2013).

²¹S. Zenitani and T. Nagai, *Phys. Plasmas* **23**, 102102 (2016).

²²A. V. Artemyev, A. I. Neishtadt, A. A. Vasiliev, and L. M. Zelenyi, *Phys. Rev. Lett.* **115**, 155001 (2015).

²³A. V. Artemyev, V. N. Lutsenko, and A. A. Petrukovich, *Ann. Geophys.* **30**, 317 (2012).

²⁴A. V. Artemyev, S. Kasahara, A. Y. Ukhorski, and M. Fujimoto, *Planet. Space Sci.* **82-83**, 134 (2013).

²⁵A. V. Artemyev and A. A. Vasiliev, *Phys. Rev. E* **91**, 053104 (2015).

²⁶Y. Uchiyama, F. A. Aharonian, T. Tanaka, T. Takahashi, and Y. Maeda, *Nature* **449**, 576 (2007).

²⁷A. Bamba, R. Yamazaki, M. Ueno, and K. Koyama, *Astrophys. J.* **589**, 827 (2003).

²⁸A. Bamba, R. Yamazaki, T. Yoshida, T. Terasawa, and K. Koyama, *Astrophys. J.* **621**, 793 (2005).

²⁹A. Bamba, R. Yamazaki, and J. S. Hiraga, *Astrophys. J.* **632**, 294 (2005).